A 60-GHz Hybrid FMCW-Doppler Radar for Vibration Detection With a Robust I/Q Calibration Method

Lin Lu, Xujun Ma, Yue Liang, Zhiqiang Liu, Xiangning Fan, Lianming Li

A 60 GHz Hybrid FMCW-Doppler Radar for Vibration Detection with a Robust I/Q Calibration Method

Lin Lu, *Graduate Student Member, IEEE,* Xujun Ma, *Member, IEEE*, Yue Liang, Zhiqiang Liu, Xiangning Fan, and Lianming Li, *Member, IEEE*

***Abstract*—In the field of non-contact sensing, both the continuous-wave (CW) Doppler radar and the frequency-modulated continuous-wave (FMCW) radar have their own superiorities. A combination of these two radar modes would be a suitable choice to accommodate various application scenarios. This paper presents a 60-GHz hybrid FMCW-Doppler radar transceiver fabricated in a 65-nm CMOS process. An on-chip frequency quadrupler driven by a 15-GHz external signal source is utilized for the 60-GHz hybrid waveform generation. Based on the hybrid operating modes, a robust I/Q imbalance calibration method is also proposed. Specifically, in the Doppler radar mode, the imbalance factors are extracted by evaluating the quadrature beat signals during the FMCW period, and then the interferometry signals are calibrated to improve the detection performance. Unlike the trajectory-based ellipse-fitting method, the accuracy of the estimated imbalance factor is independent of the target displacement. Compared with the test-signal-based imbalance factors extraction ahead of the target detection, the real-time extraction during the target detection is more efficient and can also mitigate the estimation errors caused by environmental variations. With the proposed hybrid radar system and the I/Q calibration method, an 80-mm linear displacement is recovered with a 0.016-mm root mean square error (RMSE), and a periodic vibration with a 1-μm amplitude is detected with a 16.4-dB signal-to-noise ratio (SNR). Multiple-target detection is also performed in the FMCW radar mode, and the vibration trajectories are recovered accurately.**

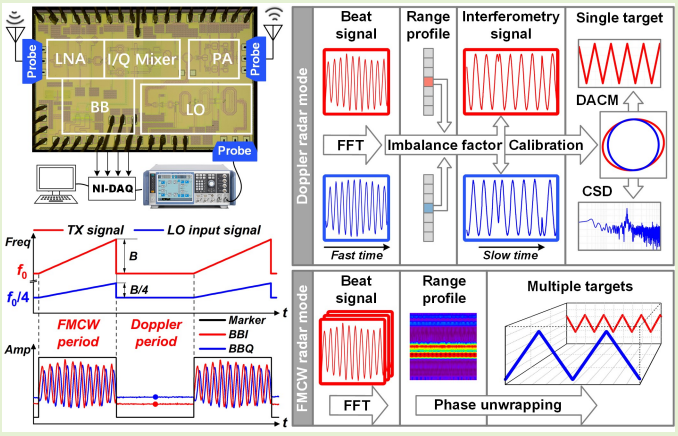

***Index Terms*—FMCW radar, Doppler radar, hybrid mode, I/Q imbalance, calibration.**

I. Introduction

MICROWAVE radars have been widely used for non-contact sensing, such as gesture recognition [1], [2], vital sign monitoring [3], [4], as well as mechanical vibration detection [5], [6]. Among different types of microwave radars, the continuous-wave (CW) Doppler radar is noted for its high precision in displacement measurement due to the sensitive phase demodulation. However, a single Doppler radar could not directly detect the absolute range due to its narrow bandwidth. To realize the target localization and distinguish multiple targets, a wideband radar such as the frequency-modulated continuous-wave (FMCW) radar is required. Based on the phase extraction method [7], [8], the FMCW radar can also be applied for displacement measurement, but the performance highly relies on the linearity of the transmitted chirp [9]. Moreover, the required data sampling frequency and computational resources of the FMCW radar are typically higher than those of the Doppler radar in displacement measurement. To leverage the strengths of these two radar modes and enhance the system adaptability to different application scenarios, a hybrid FMCW-Doppler radar combining the FMCW and CW signals for transmission would be a suitable choice. Specifically, in the scenario of multiple targets detection, the FMCW signal could be applied for vibration trajectories recovery based on the extracted phase histories, while in a single-target scenario, the CW signal is more adequate for displacement measurement with a relatively higher computational efficiency and the FMCW signal could be applied for target localization based on the beat frequency of the corresponding baseband (BB) signal.

For the implementation of the hybrid FMCW-Doppler radar, a suitable system architecture is essential. In terms of the

Manuscript received July 28, 2022; revised September 4, 2022; accepted September 4, 2022. This work was supported by the National Key R&D Program of China under Grant 2018YFE0205900, and in part by the Major Key Project of PCL under Grant PCL2021A01-2. *(Corresponding authors: Xujun Ma, Xiangning Fan, Lianming Li.)*

Lin Lu, Yue Liang, Zhiqiang Liu, Xiangning Fan, and Lianming Li are with the National Mobile Communication Research Laboratory, Southeast University, Nanjing 210096, China, and also with the Purple Mountain Laboratories, Nanjing 211100, China (e-mail: xnfan@seu.edu.cn; lianming.li@seu.edu.cn).

Xujun Ma is with the Télécom SudParis, Évry 91000, France (e-mail: xujun.ma@telecom-sudparis.eu).

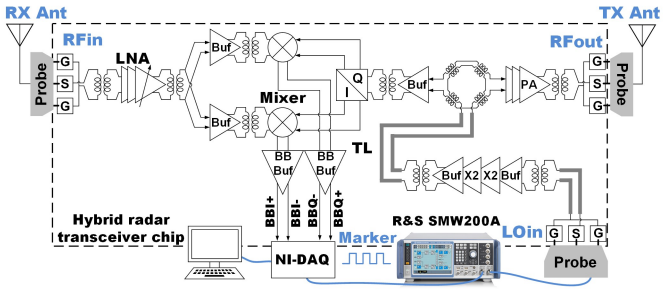

Fig. 1. Block diagram of the 60-GHz hybrid FMCW-Doppler radar system.

FMCW radar, a single-channel BB is typically applied [6], [10], while a quadrature BB is necessary for the Doppler radar to solve the null point issues [11]. To realize the hybrid operating modes without increasing the system complexity, a transceiver front end with a quadrature receiver (RX) could be shared by both the FMCW and the Doppler radar modes. In [12], a hybrid FMCW-Doppler radar based on instruments and discrete components is firstly proposed. In this work, a sequence of chirps embedded into a single-tone CW signal is provided by an external signal generator to combine the FMCW and Doppler radar modes in a time-division form. The bandwidth of the hybrid signal is 160 MHz with a 5.8-GHz central frequency. By processing different periods of the BB signals, the operating modes can be switched between the FMCW and the Doppler radar modes. In [13], a portable on-board hybrid radar system is proposed. In the FMCW radar mode, a voltage-controlled oscillator (VCO) tuned by a sawtooth waveform is utilized to generate the chirps with a bandwidth of 320 MHz around 5.8 GHz. In the Doppler radar mode, the tuning voltage of the VCO is switched to a constant value to generate a 5.8-GHz CW signal. However, due to the centimeter-level wavelength of the transmitted signals, the sensitivity of the 5.8-GHz hybrid radar systems is inadequate, especially in micrometer-level motion detections. To tackle this problem, a higher carrier frequency is required, which is favourable for improving the system sensitivity in both the FMCW and the Doppler radar modes. However, with the increase of the carrier frequency, the interconnection loss between the discrete components grows dramatically, and thus a highly integrated transceiver is preferred.

On the other hand, the orthogonality of the quadrature channels is critical for the Doppler-radar-based displacement measurement with the commonly-used demodulation algorithms such as the arctangent demodulation (ATD) [14], the differentiate and cross-multiply (DACM) [15], and the complex signal demodulation (CSD) [16]. However, due to the circuit flaws and the fabrication mismatches, I/Q imbalance is inevitable for a quadrature RX. Recently, a novel single-channel phase demodulation (ScD) technique based on signal segmentation and Hilbert transformation is proposed [17]. However, a quadrature RX is still needed for the selection of an optimal signal channel. Moreover, the computational complexity of the ScD algorithm is relatively higher. With the use of DACM or CSD algorithms, the I/Q calibration is still required for high-accuracy vibration detection. Several calibration methods have been proposed to improve the orthogonality of the I/Q signals. In [18], an extra phase shifter with control signals is utilized to measure the I/Q imbalance factors ahead of the target detection. In [19], a cross-correlation method is proposed for the phase imbalance calibration, while extra hardware and testing signals are still required to measure the amplitude imbalance factor. Clearly, these calibration methods are inconvenient and the pre-measured imbalance factors are susceptible to environmental variations, e.g., temperature fluctuation [20]. In [21] and [22], ellipse-fitting methods are proposed to estimate the I/Q imbalance factors. However, the performance of these methods highly depends on the quality of the I/Q trajectory. A poor signal-to-noise ratio (SNR) or a short arc length caused by a small displacement could both fail the fitting process. As mentioned above, both the pre-measured imbalance factors based on extra testing signals and the ellipse-fitting methods based on the I/Q trajectory are not reliable enough, and thus a more robust calibration method is required.

In this paper, a 60-GHz hybrid FMCW-Doppler radar system with a robust I/Q calibration method is proposed. The transceiver chip is fabricated in a 65-nm CMOS process. A hybrid FMCW-CW signal around 15 GHz is generated by an external signal generator and then converted to 60 GHz by an on-chip frequency quadrupler. Benefiting from the short wavelength of the transmitted signal, micrometer-level displacement could be detected by the proposed hybrid radar. Based on the hybrid operating modes, a robust I/Q calibration method is also demonstrated. By extracting the imbalance factors from the quadrature beat signals during the target detection, the estimation error caused by environmental variations could be mitigated. Compared with the test-signal-based imbalance factors extraction ahead of the target detection, the proposed method is more reliable and efficient. In addition, the accuracy of the estimated imbalance factors is insusceptible to the arc length of the I/Q trajectory, which is more reliable in small displacement measurements compared with the ellipse-fitting method.

This paper is organized as follows. In Section II, the implementation of the hybrid FMCW-Doppler radar system is demonstrated. In Section III, the theory of the hybrid-radar-based I/Q imbalance calibration is proposed and analyzed in simulations. The experiments and results of the mechanical vibration detections are presented in Section IV. The conclusion is made in Section V.

II. System Implementation

A. System Architecture and Operating Principle

The block diagram of the proposed hybrid radar system is shown in Fig. 1. It consists of a 60-GHz homodyne radar transceiver chip, two horn antennas connected to the transmitter (TX) and the RX via coaxial cables and GSG probes, and a vector signal generator (R&S SMW200A). A hybrid FMCW-CW signal around 15 GHz is generated by SMW200A and then converted to 60 GHz by an on-chip frequency quadrupler. After that, the hybrid signal is injected into the TX and the quadrature generation module respectively via the transmission line (TL) and the transformer-based power divider. In the TX, the hybrid signal is amplified by a three-stage power amplifier (PA) and transmitted by the TX antenna. The reflected signal is received by the RX antenna and amplified by

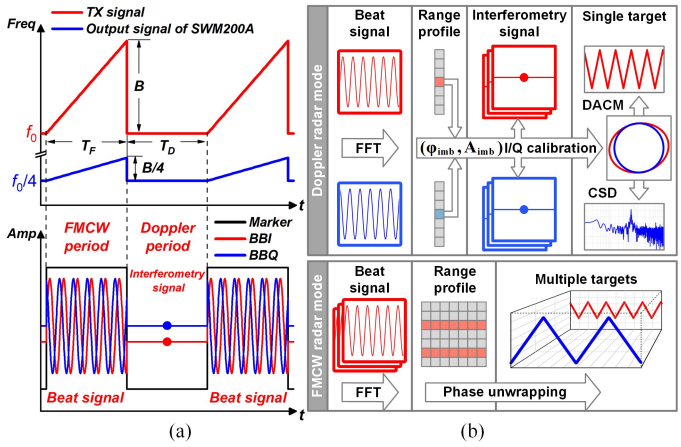

Fig. 2. (a) Diagram of the transmitted signal, the markers, and the corresponding BB signals during different periods. (b) Hybrid radar operating principle.

a three-stage low noise amplifier (LNA). Then the RF signal is down-converted by a passive I/Q mixer to generate the quadrature BB signals, which are sampled by a data acquisition module (DAQ) for digital signal processing. A square-wave marker is also provided by the SMW200A to label different transmission periods of the hybrid signals, and thus the BB signals could be separated for further processing in the FMCW and the Doppler radar modes.

The time-frequency configuration of the hybrid signal generated by SMW200A and the transmitted hybrid signal are shown in Fig. 2(a), where f_0 is the frequency of the transmitted single-tone signal during the Doppler period as well as the initial frequency of the chirp, B is the chirp bandwidth, T_F and T_D are the duration time of the alternated FMCW and Doppler periods, respectively. The hybrid BB signals and the marker are also demonstrated in Fig. 2(a). The corresponding BB signals during the FMCW and the Doppler periods are named the beat signals and the interferometry signals [12], respectively.

As shown in Fig. 2(b), the operating mode of the hybrid radar could be switched for different detection scenarios. For the single target detection, the Doppler radar mode is applied. In this operating mode, the I/Q imbalance factors are firstly extracted from the quadrature beat signals, and then the interferometry signals are calibrated to improve the detection performance. Specifically, according to the marker edges, the quadrature beat signals are extracted and processed by fast Fourier transform (FFT). Then the range profiles are obtained and the I/Q imbalance factors are extracted from the range bins in which the target is located. With the estimated amplitude imbalance factor A_{imb} and phase imbalance factor φ_{imb}, the interferometry signals are calibrated and the demodulation algorithms such as DACM and CSD are utilized for vibration information recovery. In detections of mechanical vibrations or vital signs, the relatively low-speed target could be regarded as stationary during the millisecond-level T_F and T_D, and the interferometry signal during adjacent Doppler periods could be regarded as a constant value. Thus, a sampling frequency as low as $1/(T_F + T_D)$ is adequate for the interferometry signals extraction without inducing significant signal distortion. The procedure of the I/Q imbalance factors extraction and calibration will be demonstrated in more details in Section III. For multiple-target detection, the FMCW radar mode is applied.

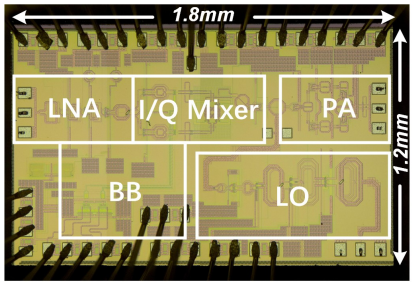

Fig. 3. Micrograph of the 60-GHz hybrid radar transceiver chip fabricated in a 65-nm CMOS process.

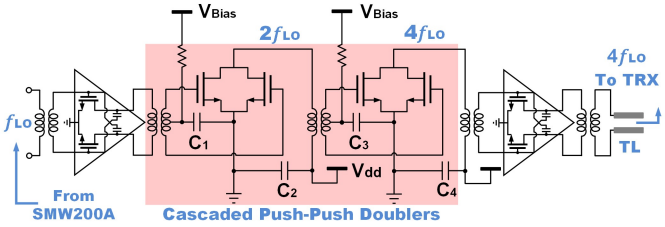

Fig. 4. Schematic of the frequency quadrupler based on cascaded push-push doublers.

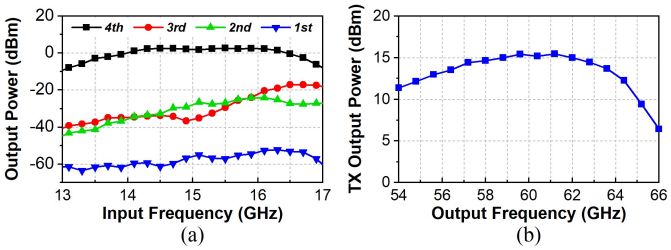

Fig. 5. (a) Measured output power of the frequency quadrupler with a -17-dBm input power. (b) Measured output power of the TX.

In this mode, the successive frames of beat signals along the slow time are extracted from a single BB channel. FFT is utilized to process each frame respectively, and the range bins of the targets could be confirmed. Then the phase history is extracted from the corresponding range bins and unwrapped for the vibration trajectories recovery [7]. It should be noted that the clock synchronization of the DAQ and SMW200A is necessary to eliminate the accumulated phase errors in the FMCW radar mode [23].

B. Module Design and Performance

Fabricated in a 65-nm CMOS process, the micrograph of the proposed hybrid radar transceiver chip is shown in Fig. 3. The chip consists of the local oscillator (LO), the TX, and the RX modules, occupying a size of 1.8 mm×1.2 mm.

In the millimeter-wave frequency bands, the implementation of a high-performance signal source with a wide frequency tuning range and low phase noise is challenging [24]. Alternatively, a low-frequency signal source cascaded with a frequency multiplier is quite suitable for high-frequency signal generation. As shown in Fig. 4, the LO module consists of the common-source (CS) amplifiers based on the capacitive neutralization technique [25] and a frequency quadrupler based on cascaded push-push doublers. As mentioned in [26], central capacitors C_1 and C_3 are utilized to improve the conversion gain and efficiency of the push-push doublers. With a -17-dBm

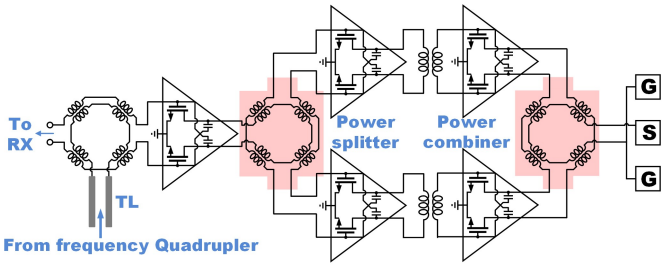

Fig. 6. Schematic of the three-stage PA based on CS amplifiers.

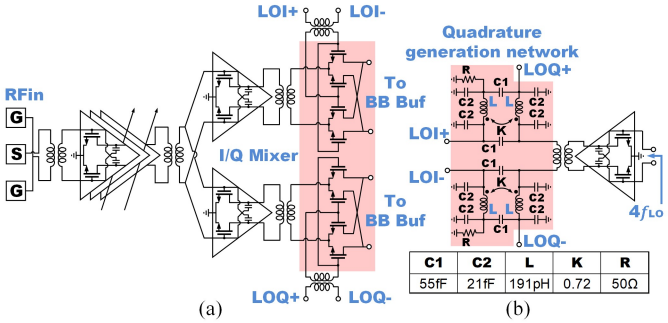

Fig. 7. Design details of the RX. (a) Schematic of the LNA and passive mixers. (b) Schematic of the transformer-based quadrature generation network.

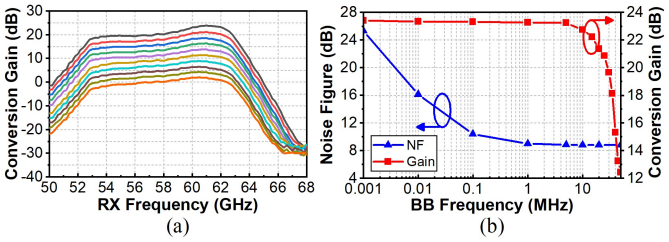

Fig. 8. (a) Measured conversion gains of the RX with a fixed 1-kHz BB frequency. (b) The simulated RX noise figure with a fixed 60-GHz RF input and the measured RX conversion gain.

fundamental input signal varying from 13 to 17 GHz, the measured output powers of the frequency quadrupler at different harmonics are shown in Fig. 5(a). The maximum conversion gain of the 4th harmonic is 19.6 dB with a 3-dB bandwidth from 56 to 66 GHz, and the harmonic rejection is better than 29 dBc at 60 GHz.

In the TX, a three-stage PA based on capacitive neutralized CS amplifiers and inter-stage impedance matching networks is demonstrated in Fig. 6. To enhance the output power and achieve a compact layout, distributive parallel power splitting and combining networks [27] are applied. With the -17-dBm input signal of the frequency quadrupler varying from 13.5 to 16.5 GHz, the measured TX output power is shown in Fig. 5(b). The saturated output power is 15.3 dBm with a 3-dB bandwidth from 55.5 to 64.5 GHz.

As shown in Fig. 7(a), in the RX, a three-stage LNA with variable power gains is designed. To accommodate the variations of the reflected signal power in different application scenarios, 10 levels of power gain with about a 2-dB step are applied. The output RF signal of the LNA is then evenly split for the I/Q down conversions. To compensate for the insertion loss of the power splitter, the split RF signals are driven by the CS buffers before being injected into the I/Q down-conversion mixers. To reduce the influence of the flicker noise on the

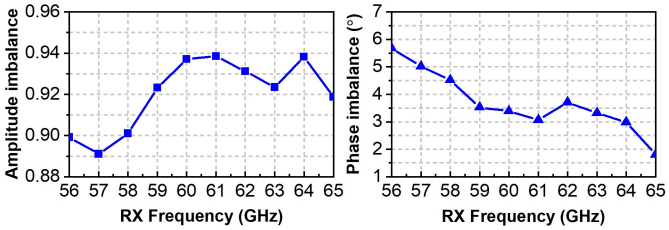

Fig. 9. Measured I/Q imbalance factors with a fixed 1-kHz BB frequency. (a) Amplitude imbalance factors. (b) Phase imbalance factors.

low-frequency BB signals, passive down-conversion mixers are utilized [28]. For the quadrature LO signals generation, a differential transformer-based quadrature generation network with a coupling factor enhancement technique is applied [29], and the key design parameters are listed in Fig. 7(b).

To evaluate the RX performance, the frequency of the BB signal is fixed at 1 kHz by keeping a 1-kHz frequency offset between f_{RX} and $4f_{LO}$, where f_{RX} and f_{LO} are the input frequencies of the LNA and the quadrupler, respectively. The measured variable conversion gains of the RX chain from the LNA input to the BB output are shown in Fig. 8(a). Within the operating frequency band, the variable conversion gains vary from 2 to 24 dB, with the corresponding input 1-dB compression point (IP_{1dB}) varying from -16 to -30 dBm. With a fixed 60-GHz RF input and the maximum gain level of the LNA, the simulated noise figure versus the BB frequency is shown in Fig. 8(b). The measured RX conversion gain with a 3-dB bandwidth of 25 MHz is also shown in Fig. 8(b).

With different f_{RX}, the BB signals in the quadrature channels are digitalized and further processed by FFT for the I/Q imbalance evaluation. As shown in Fig. 9, from 56 to 65 GHz, the amplitude imbalance varies from 0.891 to 0.938, and the phase imbalance varies from 1.8 ° to 5.6 °. Note that the pre-measured imbalance factors might deviate from those during the target detection due to environmental variations such as temperature fluctuation, and thus a more reliable method to estimate the I/Q imbalance factors is required.

III. Hybrid-Radar-Based I/Q Calibration

A. Theory

To better comprehend the hybrid-radar-based I/Q calibration method, the beat signals during the FMCW periods and the interferometry signals during the Doppler periods are analyzed separately. Given a single-point scatter model with imbalanced I/Q channels, the normalized quadrature interferometry signals during the Doppler period could be expressed as:

$$Int_I(\tau)' = A_{imb}\sin\left[4\pi d(\tau)/\lambda + \theta + \varphi_{imb}\right] + DC_I, \quad (1)$$

$$Int_Q(\tau)' = \cos\left[4\pi d(\tau)/\lambda + \theta\right] + DC_Q, \quad (2)$$

where A_{imb} and φ_{imb} are the amplitude and phase imbalance factors, respectively, τ is the slow time, λ is the wavelength of the transmitted signal with a frequency of f_0, $d(\tau)$ is the target displacement in the slow-time domain, θ is a constant phase shift caused by the signal transmission, DC_I and DC_Q are the DC offsets of the I/Q channels, respectively.

The normalized beat signals during one FMCW period could

be expressed as:

$$Beat_I(t)' = A_{imb}\sin\left[\omega(\tau)\cdot t+\varphi(\tau)+\varphi_{imb}-\varphi_r(\tau)\right], \quad (3)$$

$$Beat_Q(t)' = \cos\left[\omega(\tau)\cdot t+\varphi(\tau)-\varphi_r(\tau)\right], \quad (4)$$

$$\omega(\tau) = 4\pi B\cdot\left[D_t+d(\tau)\right]/(c\cdot T_F), \quad (5)$$

$$\varphi(\tau) = 4\pi f_0\cdot\left[D_t+d(\tau)\right]/c, \quad (6)$$

$$\varphi_r(\tau) = 4\pi B\cdot\left[D_t+d(\tau)\right]^2/(c^2\cdot T_F), \quad (7)$$

where t is the fast time, D_t is the distance between the target and the radar, c is the speed of light, and $\varphi_r(\tau)$ is the residual phase which can be neglected for short-range detection [30]. For low-speed target detection, the variation of $d(\tau)$ can be typically neglected during a millisecond-level FMCW period, thus $\omega(\tau)$ and $\varphi(\tau)$ can be regarded as constant values.

As shown in (3) and (4), the phase and amplitude differences between the imbalanced quadrature beat signals could be extracted directly by FFT, and thus the targeted imbalance factors could be obtained. With the extracted imbalance factors, the I/Q calibration matrix could be generated and the imbalanced interferometry signals could be calibrated as:

$$\begin{bmatrix} Int_{Icali}(\tau) \\ Int_{Qcali}(\tau) \end{bmatrix} = \begin{bmatrix} 1/A_{imb} & 0 \\ -\tan(\varphi_{imb})/A_{imb} & 1/\cos(\varphi_{imb}) \end{bmatrix}\begin{bmatrix} Int_I(\tau)' \\ Int_Q(\tau)' \end{bmatrix}$$

$$= \begin{bmatrix} \sin[4\pi d(\tau)/\lambda+\theta+\varphi_{imb}]+DC_I' \\ \cos[4\pi d(\tau)/\lambda+\theta+\varphi_{imb}]+DC_Q' \end{bmatrix}, \quad (8)$$

$$\begin{bmatrix} DC_I' \\ DC_Q' \end{bmatrix} = \begin{bmatrix} DC_I/A_{imb} \\ -\tan(\varphi)\cdot DC_I/A_{imb}+DC_Q/\cos(\varphi) \end{bmatrix}, \quad (9)$$

where $Int_{Icali}(\tau)$ and $Int_{Qcali}(\tau)$ are the calibrated interferometry signals without I/Q imbalance.

B. Simulations

1) *I/Q imbalance factors extraction*

To investigate the effectiveness of the real-time I/Q imbalance factors extraction, simulations are performed by involving a vibrating target with a sinusoidal motion for detection. The imbalanced beat signals during the n-th FMCW period could be expressed as:

$$Beat_{I\_n}(t)' = A_{imb}\sin\left[\omega_n(t)\,t+\varphi_n(t)+\varphi_{imb}\right], \quad (10)$$

$$Beat_{Q\_n}(t)' = \cos\left[\omega_n(t)\,t+\varphi_n(t)\right], \quad (11)$$

$$\omega_n(t) = \frac{4\pi B\left\{D_t+A_t\sin\left[2\pi f_t((n-1)\cdot(T_D+T_F)+t)\right]\right\}}{c\cdot T_F}, \quad (12)$$

$$\varphi_n(t) = \frac{4\pi f_0\left\{D_t+A_t\sin\left[2\pi f_t((n-1)\cdot(T_D+T_F)+t)\right]\right\}}{c}, \quad (13)$$

where A_t and f_t are the vibration amplitude and frequency of the sinusoidal target motion, respectively, and $t\in[0,T_F]$.

The key simulation parameters are shown in Table I. The I/Q mismatch is introduced to the simulations by setting the imbalance factors as 1.2 (A_{imb}) and 5° (φ_{imb}), respectively. The distance of the target is set as 2.2 m and the beat frequency could be derived by:

TABLE I
SIMULATION PARAMETERS

f_0	B	T_F, T_D	A_{imb}	φ_{imb}	D_t
59.68 GHz	640 MHz	2 ms	1.2	5 °	2.2 m

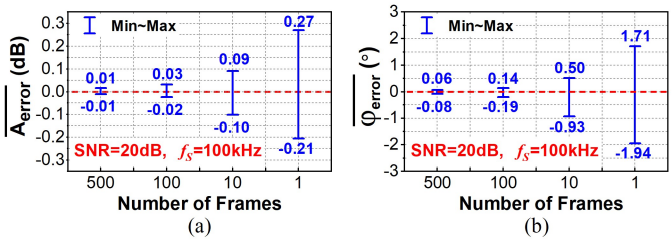

Fig. 10. Distributions of the simulated mean errors obtained with different numbers of frames. (a) Mean errors of the amplitude imbalance factors. (b) Mean errors of the phase imbalance factors.

$$f_b = 2D_t\cdot B/(c\cdot T_F). \quad (14)$$

With a 640-MHz chirp bandwidth (B) and a 2-ms chirp duration time (T_F), f_b is estimated as 4.7 kHz.

The amplitude of the sinusoidal motion is firstly set as 5 mm with a vibration frequency of 3 Hz. White Gaussian noise with the same power level is added to the quadrature channels. For clarity, the SNR mentioned in the simulation is defined as:

$$SNR = 10\log_{10}(P_{Beat-Q}/P_{noise}), \quad (15)$$

where $P_{Beat\text{-}Q}$ is the power level of the beat signal in channel Q, and P_{noise} is the power level of the added white Gaussian noise. To reduce the influence of the white noise on the estimation accuracy, the mean values of the imbalance factors extracted from several frames of quadrature beat signals could be applied. With a 100-kHz sampling frequency, the former N frames of the quadrature beat signals are extracted and processed by FFT, respectively, and N groups of estimated imbalance factors (A'_{imb_i} and φ'_{imb_i}, $i\in[1,N]$) could be obtained. The amplitude and phase errors could be represented as:

$$A_{error} = 20\log_{10}(A'_{imb\_i}/A_{imb}),\ \varphi_{error} = \varphi'_{imb\_i}-\varphi_{imb}, \quad (16)$$

and the mean values of the extracted imbalance factors as well as the mean errors could be represented as:

$$\overline{A'_{imb}} = (\sum_{i=1}^{N}A'_{imb\_i})/N,\ \overline{\varphi'_{imb}} = (\sum_{i=1}^{N}\varphi'_{imb\_i})/N, \quad (17)$$

$$\overline{A_{error}} = 20\log_{10}(\overline{A'_{imb}}/A_{imb}),\ \overline{\varphi_{error}} = \overline{\varphi'_{imb}}-\varphi_{imb}. \quad (18)$$

To evaluate the influence of the utilized frame number N on the estimation accuracy, simulations are performed with different N (500, 250, 100, and 1) for comparison. With a 20-dB SNR, simulations are performed 100 times for each frame number, and 100 groups of mean errors are obtained, respectively. The distributions of the mean errors are shown in Fig. 10(a) and (b). With the increased number of utilized frames, the estimation accuracy is improved. To balance the computational efficiency and estimation accuracy, a moderate number of frames should be applied. In the following simulations and experiments, the utilized frame number for imbalance factors extraction is fixed at 100. Given a 4-ms (T_F+T_D) repetition interval of the FMCW period, the utilized

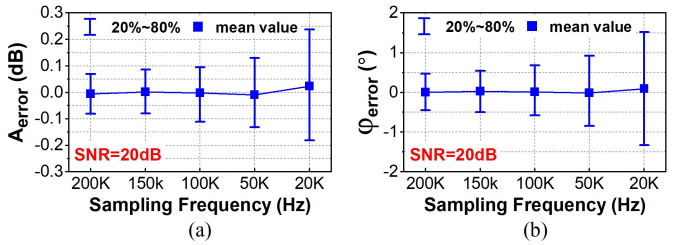

Fig. 11. Simulated estimation errors of the I/Q imbalance factors with different sampling frequencies. (a) Amplitude errors. (b) Phase errors.

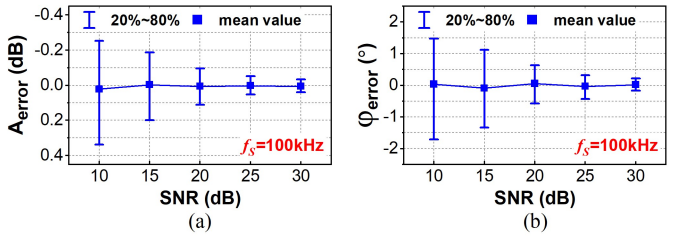

Fig. 12. Simulated estimation errors of the I/Q imbalance factors with different SNRs. (a) Amplitude errors. (b) Phase errors.

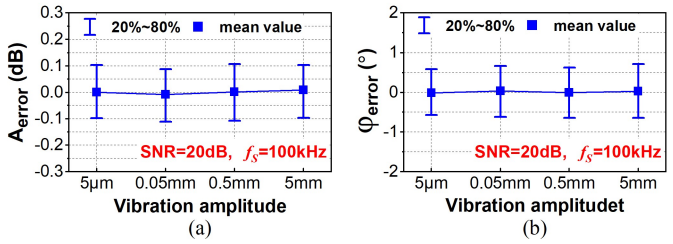

Fig. 13. Simulated estimation errors of the I/Q imbalance factors with different target vibration amplitudes. (a) Amplitude errors. (b) Phase errors.

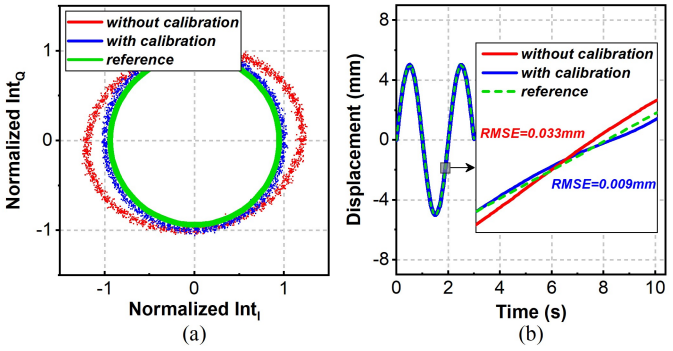

Fig. 14. Simulation results of a 0.5-Hz sinusoidal motion with an amplitude of 5 mm (SNR: 30 dB). (a) I/Q trajectories of the quadrature interferometry signals with a 10-s data sampling. A unit circle (green line) is applied for reference. (b) Recovered vibration trajectories.

100 frames of beat signals could be extracted with only a 0.4-s sampling duration.

In addition, the influence of the sampling frequency on the estimation accuracy is also investigated. With different sampling frequencies from 20 to 200 kHz, the former 100 frames of the quadrature beat signals are sampled and 100 groups of the I/Q imbalance factors are extracted, respectively. The 20% and 80% quantiles of the estimation errors as well as the mean errors are shown in Fig. 11(a) and (b). Clearly, a higher sampling frequency is favorable for improving the estimation accuracy, and the utilization of the mean values could further reduce the estimation errors. Considering the computational efficiency, a moderate sampling frequency of

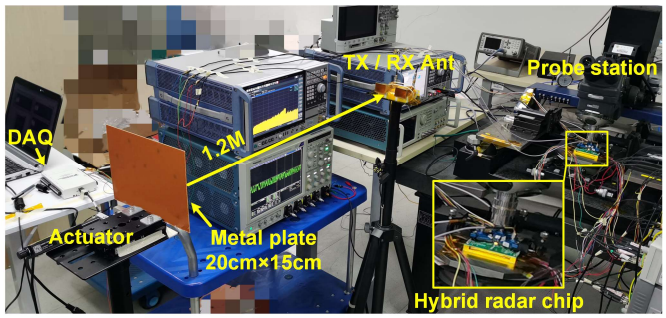

Fig. 15. Experimental setup of the probe-station-based hybrid radar system for single target detection.

100 kHz is applied for the beat signals sampling.

As shown in Fig. 12(a) and (b), simulations are also performed with different SNRs to evaluate the robustness of the proposed method against noise. With an SNR over 20 dB, the 20% and 80% quantiles of the amplitude and phase error lie within ±0.1 dB and ±0.6 º, respectively. The mean errors are extremely small, and thus the mean values ($\overline{A'_{imb}}$ and $\overline{\varphi'_{imb}}$) could be utilized for the I/Q imbalance factors estimation.

With a fixed SNR of 20 dB, simulations are also performed with different vibration amplitudes, i.e., 5 μm, 0.05 mm, 0.5 mm, and 5 mm. The vibration frequency is fixed at 3 Hz and a full motion cycle is experienced during the 100-frame quadrature beat signals extraction. The estimation errors are shown in Fig. 13(a) and (b). Clearly, the accuracy of the estimated imbalance factor is independent of the target vibration amplitude, making the proposed method much more reliable compared with the ellipse-fitting method, especially in small displacement measurement with a short I/Q trajectory.

In addition, it should be noted that the imbalance factors are not always constant within the chirp bandwidth, introducing more challenges to the imbalance factors estimation. To reduce the variations of the imbalance factors within the chirp frequency range, a moderate 640-MHz bandwidth centered at 60 GHz is utilized in the following experiments.

2) *Motion trajectory recovery*

Given a 0.5-Hz sinusoidal motion with an amplitude of 5 mm, simulations are performed for motion trajectory recovery. With a 30-dB SNR, the former 100 frames of quadrature beat signals are extracted with a 100-kHz sampling frequency for the imbalance factors extraction. The estimated imbalance factors are 1.198 and 4.997º, respectively. Then the quadrature interferometry signals are sampled with a much lower sampling frequency of 250 Hz ($1/(T_F+T_D)$), and the calibration algorithm in (8) is applied. The I/Q trajectory of the original interferometry signals as well as that of the calibrated ones is shown in Fig. 14(a). As shown in Fig. 14(b), compared with the referenced vibration trajectory, the root mean square error (RMSE) of the recovered trajectory by the DACM algorithm is improved from 0.033 mm to 0.009 mm with the proposed I/Q calibration method.

IV. Experiments and Results

A. Detection of A Single Target

In the scenario of a single-target detection, the displacement history was recovered by the Doppler radar mode. The setup of

TABLE II
PARAMETERS IN RADAR EQUATION

P_t	G_t, G_r	λ	σ	D_t	P_L
15 dBm	20 dBi	5 mm	20 cm×15 cm	1.2 m	-12 dB

a probe-station-based hybrid radar system for vibration detection is shown in Fig. 15. The radar transceiver system was mounted on the probe station, and the TX/RX horn antennas were connected to the transceiver chip by the coaxial cables and the probes. A 20 cm×15 cm metal reflector controlled by a linear actuator was placed 1.2 m away from the antennas for detection. The received signal power P_r could be derived according to the radar equation [31]:

$$P_r = P_t + G_t + G_r + 10\log_{10}[\frac{\lambda^2\sigma}{(4\pi)^3 D_t^4}] + P_L, \qquad (19)$$

where P_t is the output power of the TX, G_t and G_r are antenna gains, λ is the wavelength, σ is the radar cross section, D_t is the distance between the target and the antennas, and P_L is the power loss caused by the coaxial cables and the probes. Based on the parameters listed in Table II, P_r is estimated as -54 dBm. The setup of the transmitted hybrid signal is consistent with the parameters in Table I. Considering the transmission delay caused by the 1-m coaxial cables in the TX and RX chains, the length of the one-way signal transmission path is about 2.2 m, and the beat frequency is estimated as 4.7 kHz.

According to the RX sensitivity calculation formula, the SNR of the beat signals could be estimated by:

$$SNR(dB) = P_r(dBm) - KTB_{BB}(dBm) - NF(dB), \qquad (20)$$

where KT is the input thermal noise floor per unit bandwidth, B_{BB} is the baseband bandwidth of the RX, and NF is the noise figure. According to the measured and simulated results in Fig. 8(b), the noise figure at 4.7 kHz is about 18 dB. With a BB bandwidth of 25 MHz, the SNR is estimated as 28 dB, which is adequate for the proposed I/Q calibration method.

To evaluate the practical performance of the hybrid radar system with the proposed I/Q calibration method, the linear actuator was programmed to provide periodic motions for detection. Firstly, a 0.2-Hz vibration with a 5-mm amplitude was provided. In order to exhibit the BB signals and the marker completely, the quadrature signals and the marker were sampled for 10 s with a fixed 100-kHz sampling frequency. A segment of the signals is plotted in Fig. 16(a) and the zoomed-in view is shown in Fig. 16(b), where the beat signals, the interferometry signals, and the marker could be clearly identified. With the obtained BB signals, the detailed data processing flow for the calibration of the quadrature interferometry signals is shown in Fig. 17. According to the rising and falling edges of the marker, the beat signals and the interferometry signals could be separated, and then the former 100 frames of quadrature beat signals were extracted for I/Q imbalance factors extraction. Specifically, FFT was utilized to process each frame of beat signal and 100 groups of I/Q imbalance factors could be obtained, and then the mean values of these imbalance factors were applied to the I/Q calibration matrix in (8). Meanwhile, the interferometry signals were down-sampled and reconstructed. Specifically, with a 1-ms

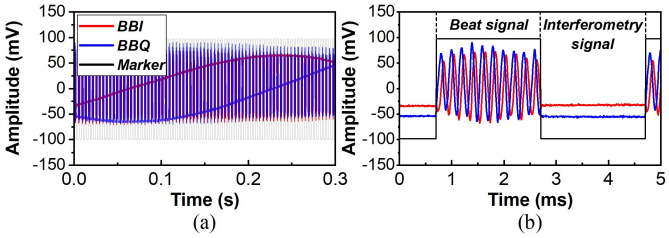

Fig. 16. (a) Sampled BB signals from the quadrature channels as well as the markers. (b) Zoomed-in view with more details.

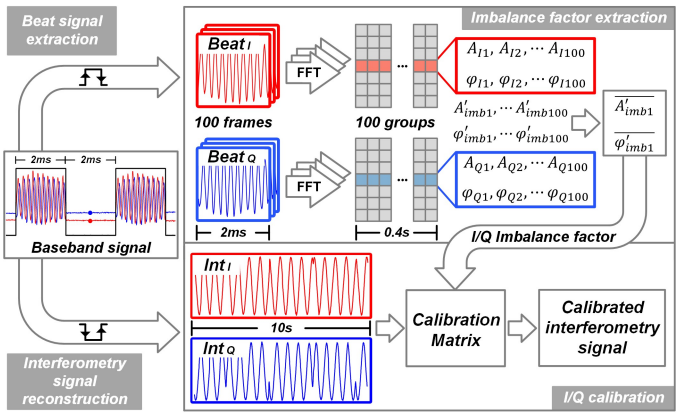

Fig. 17. Data processing flow for the calibration of the quadrature interferometry signals.

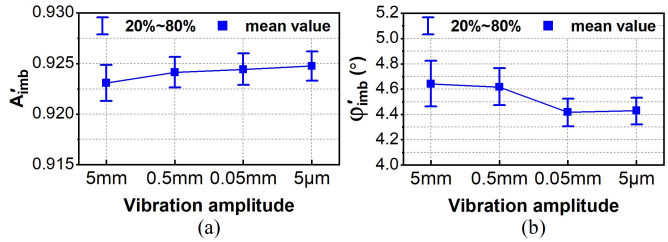

Fig. 18. Measured I/Q imbalance factors with different vibration amplitudes. (a) Amplitude imbalance factors (b) Phase imbalance factors.

delay after every falling edge of the marker, a pair of samples were extracted from the quadrature BB signals to construct the low-frequency interferometry signals, greatly reducing the data volume and improving the computational efficiency in the following signal processing. With the reconstructed interferometry signals and the calibration matrix, the calibrated interferometry signals could be obtained for high-accuracy displacement measurement.

Furthermore, with different target vibration amplitudes of 5 mm, 0.5 mm, 0.05 mm, and 5 μm, the 20% and 80% quantiles of the obtained 100 groups of imbalance factors as well as the mean values are shown in Fig. 18(a) and (b), where the distributions of $\overline{A'_{imb}}$ vary from 0.923 to 0.924 and the distributions of $\overline{\varphi'_{imb}}$ vary from 4.42° to 4.63°. The tiny deviations of the averaged imbalance factors prove that the accuracy of the proposed method is independent of the target displacement, which is more robust compared with the ellipse-fitting method.

With a fixed 5-mm vibration amplitude for detection, the I/Q trajectory of the reconstructed 10-s quadrature interferometry signals is shown in Fig. 19(a). Due to the amplitude and phase

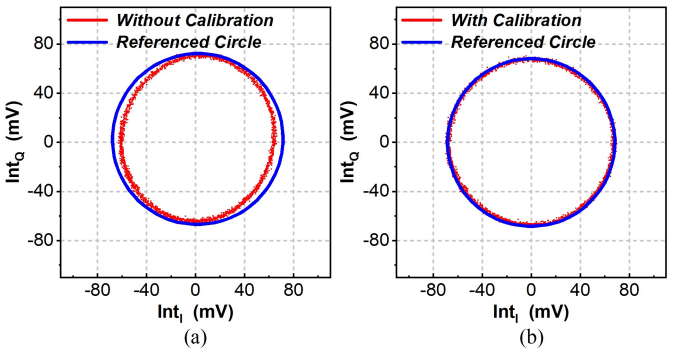

Fig. 19. I/Q trajectories of the quadrature interferometry signals (Target vibration amplitude: 5 mm). (a) Without I/Q calibration. (b) With I/Q calibration.

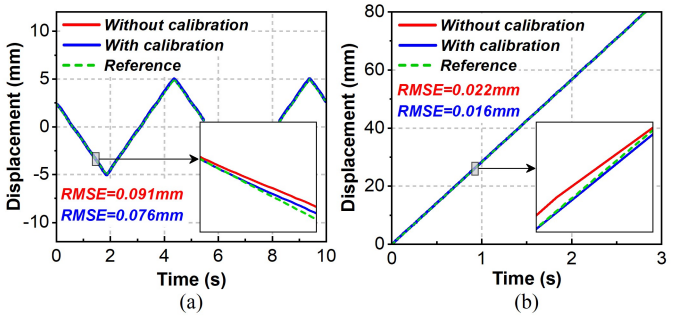

Fig. 20. Measurement results of the single-target detections. (a) 0.2-Hz periodic vibration with a 5-mm amplitude. (b) Linear motion with an 80-mm displacement.

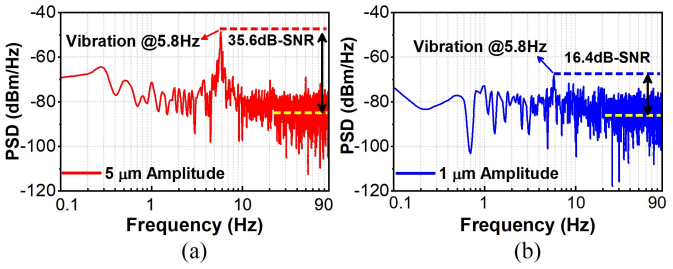

Fig. 21. PSD results of the mechanical vibration detections with different actuator setups. (a) 5.8-Hz periodic vibration with 5-μm amplitude. (b) 5.8-Hz periodic vibration with 1-μm amplitude.

imbalance, the trajectory deviates from the ideal circle. Then the estimated imbalance factors ($\overline{A'_{imb}}$ = 0.923, $\overline{\varphi'_{imb}}$ = 4.63º) were applied to calibrate the imbalanced interferometry signals. As shown in Fig. 19(b), after the DC offset cancellation, the calibrated I/Q trajectory matches well with the referenced circle, proving that the imbalance factors are correctly estimated and the calibration method functions well. As shown in Fig. 20(a), to further verify the performance improvement with the proposed I/Q calibration method, the vibration trajectories are recovered by the DACM algorithm with and without I/Q calibration, respectively. Taking a 0.2-Hz triangle waveform with a 5-mm amplitude as the referenced trajectory, the RMSE of the recovered trajectory is improved from 0.091 mm to 0.076 mm with I/Q calibration. The relatively large error is mainly caused by the inertia-induced vibration of the metal plate as well as the nonlinear motion of the actuator around the position of the maximum displacement. To mitigate the errors induced by the inaccuracy of the referenced trajectory, a linear motion with a large displacement of 80 mm was also produced by the actuator for detection. With I/Q calibration, the RMSE of the

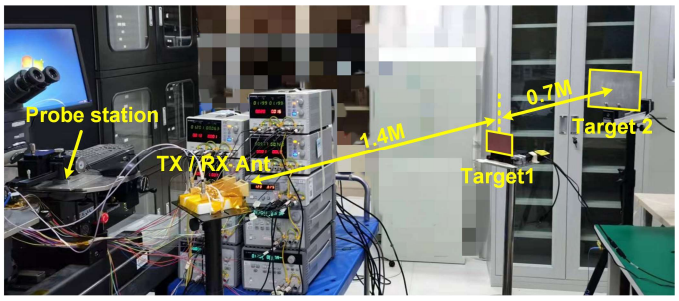

Fig. 22. Experimental setup of the probe-station-based hybrid radar system for multiple targets detection.

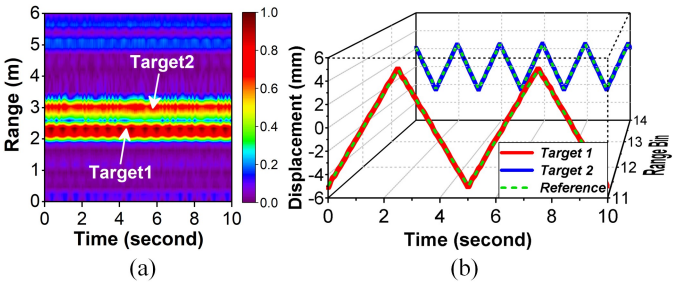

Fig. 23. (a) Range profiles of two vibrating targets with a 0.7-m separation. (b) Recovered vibration trajectories of two targets by the FMCW radar mode.

recovered trajectory is improved from 0.022 mm to 0.016 mm as shown in Fig. 20(b).

To further explore the detection sensitivity of the proposed hybrid radar, 5.8-Hz periodic vibrations with 5-μm and 1-μm amplitudes were generated by the linear actuator for detection, respectively. The CSD algorithm was applied and the power spectral densities (PSD) of the calibrated complex interferometry signals are shown in Fig. 21. The vibration signals at 5.8 Hz could be recognized clearly with SNRs of 35.6 dB (5 μm) and 16.4 dB (1 μm), respectively.

B. Detection of Multiple Targets

In the scenario of multiple-target detection, the FMCW radar mode was applied. Calculated by $c/(2B)$, the range resolution in the FMCW radar mode is about 23.4 cm. To distinguish different targets from different ranges, the distance between the targets along the radar line-of-sight (LOS) should be larger than 23.4 cm. The setup of the multiple-target detection is shown in Fig. 22. Two metal plates driven by linear actuators were placed along the radar LOS. Target 1 was placed 1.4 m away from the antennas and vibrated at 0.2 Hz with a 5-mm amplitude. Target 2 was placed 0.7 m behind target 1 and vibrated at 0.5 Hz with a 2.5-mm amplitude. As the displacement information could be recovered from a single BB channel in the FMCW radar mode, the calibration of the I/Q imbalance is not needed. In the experiment, the BB signals of channel I were sampled for 10 s with a 100-kHz sampling frequency, and 2500 frames of beat signals were extracted. After applying FFT to each frame, the stacked range profiles along the slow time were obtained as shown in Fig. 23(a). These two targets could be clearly recognized at the distance of 2.34 m (range bin 10) and 3.04 m (range bin 13), respectively. It should be noted that the detected range information also includes the length of the 1-m coaxial cable. The actual lengths of the one-way signal transmission paths between the targets

TABLE III
PERFORMANCE COMPARISONS

Ref	Freq (GHz)	Mode	Error/ Displacement	S [a] (μm)	D [b] (m)	I/Q Calibration
[21]	2.4	Doppler	0.97 mm / 4 cm	–	1	ellipse-fitting
[12]	5.8	Hybrid	1 mm / 1.5 cm	–	1.2	–
[8]	24	FMCW	25 μm / 0.8 cm	–	1.4	–
[32]	60	Doppler	–	20	0.3	–
[6]	79	FMCW	16.1 μm / 4 cm	–	0.3	–
[33]	120	Doppler	13 μm / 5 cm	1	0.8	–
[34]	122	FMCW	6 μm / 3.5 cm	–	1.6	–
[19]	125	Doppler	–	0.1 [c]	1	Testing signal & cross-correlation [e]
This work	60	Hybrid	16 μm / 8 cm	1 [d]	1.2	Hybrid radar based

[a]Sensitivity. [b]Detection distance. [c]SNR=9.6 dB. [d]SNR=16.4 dB.
[e]The magnitude and phase imbalances are calibrated by extra testing signals and cross-correlation based method, respectively.

and the transceiver chip are about 2.4 m and 3.1 m, respectively, agreeing with the target locations shown in the range profiles. Then the phase information was extracted from the corresponding range bins along the slow time and the motion trajectories were recovered from the unwrapped phase history as shown in Fig. 23(b). The RMSEs of the recovered trajectories of target 1 and target 2 are 0.083 mm and 0.059 mm, respectively.

The performance comparisons between the proposed 60-GHz hybrid radar system and several relevant works are shown in Table III. Compared with the low-frequency radars, this work exhibits a better performance due to the shorter wavelength of the transmitted signal. Compared with the radars operating at higher frequencies, the performance of this work is still competitive benefiting from the effectiveness of the proposed I/Q calibration method.

V. CONCLUSION

A 60-GHz hybrid FMCW-Doppler radar system is designed in this paper. The system architecture as well as the design details are demonstrated. Based on the hybrid operating modes, a robust I/Q imbalance calibration method is proposed. By extracting the real-time imbalance factors during the target detection, the influence of the environmental variations on the imbalance factors can be mitigated, which is more credible and efficient compared with the test-signal-based imbalance factors extraction ahead of the target detection. The proposed method also shows robustness against different vibration amplitudes, which is more effective compared with the I/Q-trajectory-based ellipse-fitting method. With the proposed hybrid radar and the I/Q calibration method, an 80-mm linear displacement is recovered by the Doppler radar mode with a 0.016-mm RMSE. A periodic vibration with 1-μm amplitude is also successfully detected with a 16.4-dB SNR. Based on the FMCW radar mode, multiple-target detection is also performed, and the vibration trajectories are recovered accurately.

REFERENCES

[1] T. Fan *et al.*, "Wireless Hand Gesture Recognition Based on Continuous-Wave Doppler Radar Sensors," *IEEE Trans. Microw. Theory Techn.*, vol. 64, no. 11, pp. 4012–4020, Nov. 2016.

[2] L. Gan, Y. Liu, Y. Li, R. Zhang, L. Huang, and C. Shi, "Gesture Recognition System Using 24 GHz FMCW Radar Sensor Realized on Real-Time Edge Computing Platform," *IEEE Sens. J.*, vol. 22, no. 9, pp. 8904–8914, May 2022.

[3] A. Singh and V. M. Lubecke, "Respiratory Monitoring and Clutter Rejection Using a CW Doppler Radar With Passive RF Tags," *IEEE Sens. J.*, vol. 12, no. 3, pp. 558–565, Mar. 2012.

[4] H.-R. Chuang, H.-C. Kuo, F.-L. Lin, T.-H. Huang, C.-S. Kuo, and Y.-W. Ou, "60-GHz Millimeter-Wave Life Detection System (MLDS) for Noncontact Human Vital-Signal Monitoring," *IEEE Sens. J.*, vol. 12, no. 3, pp. 602–609, Mar. 2012.

[5] X. Ma *et al.*, "Design of a 100-GHz Double-Sideband Low-IF CW Doppler Radar Transceiver for Micrometer Mechanical Vibration and Vital Sign Detection," *IEEE Trans. Microw. Theory Techn.*, vol. 68, no. 7, pp. 2876–2890, Jul. 2020.

[6] J. Liu, Y. Li, and C. Gu, "Solving Phase Ambiguity in Interferometric Displacement Measurement With Millimeter-Wave FMCW Radar Sensors," *IEEE Sens. J.*, vol. 22, no. 9, pp. 8482–8489, May 2022.

[7] G. Wang, J.-M. Munoz-Ferreras, C. Gu, C. Li, and R. Gomez-Garcia, "Application of Linear-Frequency-Modulated Continuous-Wave (LFMCW) Radars for Tracking of Vital Signs," *IEEE Trans. Microw. Theory Techn.*, vol. 62, no. 6, pp. 1387–1399, Jun. 2014.

[8] Y. Xiong, Z. Peng, G. Xing, W. Zhang, and G. Meng, "Accurate and Robust Displacement Measurement for FMCW Radar Vibration Monitoring," *IEEE Sens. J.*, vol. 18, no. 3, pp. 1131–1139, Feb. 2018.

[9] A. Anghel, G. Vasile, R. Cacoveanu, C. Ioana, and S. Ciochina, "Short-Range Wideband FMCW Radar for Millimetric Displacement Measurements," *IEEE Trans. Geosci. Remote Sens.*, vol. 52, no. 9, pp. 5633–5642, Sep. 2014.

[10] J. Liu, Y. Li, C. Li, C. Gu, and J.-F. Mao, "Accurate Measurement of Human Vital Signs With Linear FMCW Radars Under Proximity Stationary Clutters," *IEEE Trans. Biomed. Circuits Syst.*, vol. 15, no. 6, pp. 1393–1404, Dec. 2021.

[11] A. D. Droitcour, O. Boric-Lubecke, V. M. Lubecke, J. Lin, and G. T. A. Kovacs, "Range Correlation and I/Q Performance Benefits in Single-Chip Silicon Doppler Radars for Noncontact Cardiopulmonary Monitoring," *IEEE Trans. Microw. Theory Techn.*, vol. 52, no. 3, pp. 838–848, Mar. 2004.

[12] G. Wang, C. Gu, T. Inoue, and C. Li, "A Hybrid FMCW-Interferometry Radar for Indoor Precise Positioning and Versatile Life Activity Monitoring," *IEEE Trans. Microw. Theory Techn.*, vol. 62, no. 11, pp. 2812–2822, Nov. 2014.

[13] Z. Peng *et al.*, "A Portable FMCW Interferometry Radar With Programmable Low-IF Architecture for Localization, ISAR Imaging, and Vital Sign Tracking," *IEEE Trans. Microw. Theory Techn.*, vol. 65, no. 4, pp. 1334–1344, Apr. 2017.

[14] B.-K. Park, O. Boric-Lubecke, and V. M. Lubecke, "Arctangent Demodulation With DC Offset Compensation in Quadrature Doppler Radar Receiver Systems," *IEEE Trans. Microw. Theory Techn.*, vol. 55, no. 5, pp. 1073–1079, May 2007.

[15] J. Wang, X. Wang, L. Chen, J. Huangfu, C. Li, and L. Ran, "Noncontact Distance and Amplitude-Independent Vibration Measurement Based on an Extended DACM Algorithm," *IEEE Trans. Instrum. Meas.*, vol. 63, no. 1, pp. 145–153, Jan. 2014.

[16] Y. Yan, C. Li, and J. Lin, "Effects of I/Q mismatch on measurement of periodic movement using a Doppler radar sensor," in *2010 IEEE Radio and Wireless Symposium (RWS)*, New Orleans, LA, USA, Jan. 2010, pp. 196–199.

[17] W. Xu, C. Gu and J. Mao, "Interferometric Motion Sensing With a Single-Channel Radar Sensor Based on a Novel Calibration-Free Phase Demodulation Technique," *IEEE Microw. Wirel. Compon. Lett.*, vol. 32, no. 6, pp. 807-810, June 2022.

[18] B.-K. Park, S. Yamada, and V. Lubecke, "Measurement Method for Imbalance Factors in Direct-Conversion Quadrature Radar Systems," *IEEE Microw. Wirel. Compon. Lett.*, vol. 17, no. 5, pp. 403–405, May. 2007.

[19] D. Rodriguez and C. Li, "Sensitivity and distortion analysis of a 125-GHz interferometry radar for submicrometer motion sensing applications," IEEE Trans. *Microw. Theory Techn.*, vol. 67, no. 12, pp. 5384–5395, Dec. 2019.

[20] J. Luo, A. Kortke, W. Keusgen, and M. Valkama, "A Novel Adaptive Calibration Scheme for Frequency-Selective I/Q Imbalance in Broadband Direct-Conversion Transmitters," *IEEE Trans. Circuits Syst. II Express Briefs*, vol. 60, no. 2, pp. 61–65, Feb. 2013.

[21] A. Singh *et al.*, "Data-Based Quadrature Imbalance Compensation for a CW Doppler Radar System," *IEEE Trans. Microw. Theory Techn.*, vol. 61, no. 4, pp. 1718–1724, Apr. 2013.
[22] M. Zakrzewski *et al.*, "Quadrature Imbalance Compensation With Ellipse-Fitting Methods for Microwave Radar Physiological Sensing," *IEEE Trans. Microw. Theory Techn.*, vol. 62, no. 6, pp. 1400–1408, Jun. 2014.
[23] J. Liu, C. Gu, Y. Zhang, and J.-F. Mao, "Phase Correction in Asynchronous FMCW Radar Systems for Accurate Noncontact Cardiopulmonary Monitoring," in *2021 IEEE MTT-S International Microwave Symposium (IMS)*, Atlanta, GA, USA, Jun. 2021, pp. 366–369.
[24] O. Momeni and E. Afshari, "High Power Terahertz and Millimeter-Wave Oscillator Design: A Systematic Approach," *IEEE J. Solid-State Circuits*, vol. 46, no. 3, pp. 583–597, Mar. 2011.
[25] Z. Deng and A. M. Niknejad, "A layout-based optimal neutralization technique for mm-wave differential amplifiers," in *2010 IEEE Radio Frequency Integrated Circuits Symposium*, Anaheim, CA, USA, 2010, pp. 355–358.
[26] Y. Ye, B. Yu, A. Tang, B. Drouin, and Q. J. Gu, "A High Efficiency E-Band CMOS Frequency Doubler With a Compensated Transformer-Based Balun for Matching Enhancement," *IEEE Microw. Wirel. Compon. Lett.*, vol. 26, no. 1, pp. 40–42, Jan. 2016.
[27] J. Chen and A. M. Niknejad, "A compact 1V 18.6dBm 60GHz power amplifier in 65nm CMOS," in *2011 IEEE International Solid-State Circuits Conference*, San Francisco, CA, USA, Feb. 2011, pp. 432–433.
[28] L. Chen, L. Zhang, W. Wu, L. Zhang, and Y. Wang, "A Compact 76-81 GHz 3TX/4RX Transceiver for FMCW Radar Applications in 65-nm CMOS Technology," in *2019 IEEE Radio Frequency Integrated Circuits Symposium (RFIC)*, Boston, MA, USA, Jun. 2019, pp. 311–314.
[29] J. S. Park, S. Kousai, and H. Wang, "A fully differential ultra-compact broadband transformer based quadrature generation scheme," in *Proceedings of the IEEE 2013 Custom Integrated Circuits Conference*, San Jose, CA, USA, Sep. 2013, pp. 1–4.
[30] J.-M. Munoz-Ferreras and R. Gomez-Garcia, "A Deramping-Based Multiband Radar Sensor Concept With Enhanced ISAR Capabilities," *IEEE Sens. J.*, vol. 13, no. 9, pp. 3361–3368, Sep. 2013.
[31] Changzhi Li, Xiaogang Yu, Chien-Ming Lee, Dong Li, Lixin Ran, and Jenshan Lin, "High-Sensitivity Software-Configurable 5.8-GHz Radar Sensor Receiver Chip in 0.13-um CMOS for Noncontact Vital Sign Detection," *IEEE Trans. Microw. Theory Techn.*, vol. 58, no. 5, pp. 1410–1419, May 2010.
[32] T. J. Kao, Y. Yan, T. Shen, A. Y. Chen and J. Lin, "Design and Analysis of a 60-GHz CMOS Doppler Micro-Radar System-in-Package for Vital-Sign and Vibration Detection," *IEEE Trans. Microw. Theory Techn.*, vol. 61, no. 4, pp. 1649-1659, April 2013.
[33] W. Xu, Y. Li, C. Gu and J. -F. Mao, "Large Displacement Motion Interferometry With Modified Differentiate and Cross-Multiply Technique," *IEEE Trans. Microw. Theory Techn*., vol. 69, no. 11, pp. 4879-4890, Nov. 2021.
[34] M. Pauli et al., "Miniaturized Millimeter-Wave Radar Sensor for High-Accuracy Applications," *IEEE Trans. Microw. Theory Techn*., vol. 65, no. 5, pp. 1707-1715, May 2017.

Lin Lu (Graduate Student Member, IEEE) received the B.S. degree in microelectronics from Nanjing University of Posts and Telecommunications, Nanjing, China, in 2015, and the M.S. degree in microelectronics and solid state electronics from Southeast University, Nanjing, China, in 2018, where he is currently pursuing the Ph.D. degree in circuits and systems.

Since 2018, he has been with the Integrated Communication Circuits Research Group, Southeast University. His current research interests include millimeter-wave CMOS circuit design and wireless sensing.

Xujun Ma (Member, IEEE) received the B.S. degree in information engineering and the Ph.D. degree in information and communication engineering from Southeast University, Nanjing, China, in 2014 and 2020, respectively.

Since 2020, he has been a Post-Doctoral Research Fellow with the Ambient Intelligence and Pervasive System Group, Télécom SudParis, France. His current research interests include biomedical application of microwave, millimeter-wave CMOS circuit design, and wireless sensing.

Dr. Ma was the Second-Place Award recipient of the Student Paper Competition of 2019 IEEE-IMBioC.

Yue Liang received the B.S. degree from University of Electronic Science and Technology of China, Chengdu, in 2015, and is currently pursuing the Ph.D. degree in information science and engineering in Southeast University, Nanjing, China.

Her current research interests include millimeter-wave CMOS circuit design and THz source generation.

Zhiqiang Liu received the B.S. degree in electronic information science and technology from Nanjing University of Aeronautics and Astronautics and the Ph.D. degree in electromagnetic field and microwave technology at the State Key Laboratory of Millimeter Waves in Southeast University, Nanjing, China, in 2013 and 2019, respectively.

Since 2020, he has been with Purple Mountain Laboratories. His research interests include microwave and millimeter wave circuits and systems, phased array antennas, and gap waveguide technology.

Xiangning Fan (S'99–M'05) received the B.S. and M.S. degrees both from Nanjing University of Posts and Telecommunications in 1985 and 1988, respectively. From 1997, he became a part-time Ph.D. in National Communications Research Laboratory (NCRL), Southeast University, Nanjing, China, and received the Ph.D. degree in 2005 with Grade A.

Since 1988, he has been with Southeast University and now he is a full Professor in Institute of RF-&-OE-ICs, School of Information Science and Engineering, Southeast University. He has finished more than 40 major projects of National 973 projects, National 863 Hi-Tech projects, and National Nature Science Foundation projects on RF, WSN, UWB, GNSS, and 3G/4G/5G/6G Mobile Systems, and published more than 150 papers in IEEE T-CAS I & II, IEEE Comm. Letters, IET Electronic Letters, IET Radar, Sonar & Navigation, Signal Processing, Sensor Letters, Springer AICASP, JCSC, ACES Journal, etc. with more than 120 papers being SCI/EI indexed. He has been granted 15 national invention patents. His current research interests include RF ICs, MMICs, receiver design, and signal processing of wireless and satellite systems.

Lianming Li (S'06–M'11) was born in Runan, Henan province, China, in 1978. He received the B.S. degree in physics, the M.S. degree in electrical engineering from Southeast University, Nanjing, China, in 2001 and 2004 respectively, and the Ph.D. degree from Katholieke Universiteit Leuven, Leuven, Belgium, in 2011.

From 2006 to 2011, he was a research assistant of ESAT-MICAS, Katholieke Universiteit Leuven, working on the mmWave CMOS design. Since May 2011, he has been working in the school of Information Science & Engineering, Southeast University as an Associate Professor. His present research interests focus on mmWave circuits and system design, antenna and packaging design, as well as the frequency generation circuits design.